

# Laser Pulse-Stretching Using Multiple Optical Ring-Cavities

Jun Kojima<sup>1</sup> and Quang-Viet Nguyen<sup>2</sup>

National Aeronautics and Space Administration  
Glenn Research Center  
21000 Brookpark Rd  
Cleveland OH 44135  
USA

<sup>1</sup>NRC Research Fellow

<sup>2</sup>Corresponding Author, E-mail: Quang-Viet.Nguyen@grc.nasa.gov, Fax: (216) 433-5802

## ABSTRACT

We describe a simple and passive nanosecond-long (ns-long) laser ‘pulse-stretcher’ using multiple optical ring-cavities. We present a model of the pulse-stretching process for an arbitrary number of optical ring-cavities. Using the model, we optimize the design of a pulse-stretcher for use in a spontaneous Raman scattering excitation system that avoids laser-induced plasma spark problems. From the optimized design, we then experimentally demonstrate and verify the model with a 3-cavity pulse-stretcher system that converts a 1000 mJ, 8.4 ns-long input laser pulse into an approximately 75 ns-long (FWHM) output laser pulse with a peak power reduction of 0.10X, and an 83% efficiency.

This report is a preprint of an article submitted to a journal for publication. Because of changes that may be made before formal publication, this preprint is made available with the understanding that it will not be cited or reproduced without the permission of the author.

## INTRODUCTION

Non-intrusive, laser-based optical diagnostic techniques are important in spatially and temporally resolved measurements of turbulent and chemically reacting flow processes such as combustion. In particular, spontaneous Raman scattering (SRS) spectroscopy using pulsed lasers is one of the few techniques that can provide a quantitative measurement of major chemical species concentrations and temperature in turbulent reacting flows.<sup>1-5</sup> In order to collect high-quality SRS data in gas-phase flows, high-energy pulsed lasers are required to compensate for the weak signal levels generated by the Raman effect. In the past decade, reliable high energy (and high peak power) Q-switched (QS) Nd:YAG lasers that produce circa 1 J pulses at 532 nm have been used to maximize the weak SRS signals of gas-phase molecular species (see Nguyen et al. for example).<sup>6</sup> However, high energy QS lasers often suffer from laser-induced plasma spark generation at the focused probe volume.<sup>7-9</sup> The strong optical emission from the plasma spark overwhelms the weak Raman scattering signal, making spatially resolved measurements with high energy QS Nd:YAG lasers very challenging. Previously, flashlamp-pumped dye lasers, although inconvenient to use, were often employed for SRS excitation since they produced laser pulse energies of order 1 J over several microseconds at 532 nm, avoiding the plasma spark problems inherent with QS Nd:YAG lasers.<sup>2</sup> Thus, a way of reducing the peak laser power while maintaining the total pulse energy is needed to facilitate SRS measurements in combustion environments using the readily available and convenient QS Nd:YAG laser.

The 532 nm wavelength output obtained by second harmonic generation (SHG) is a popular choice for SRS excitation. This wavelength is often used since it maximizes the weak Raman signal (compared to longer wavelength lasers) and also permits conventional visible-wavelength optics and detectors to be used. Thus a technique that reduces the peak power of the

SHG output of a QS Nd:YAG laser while maintaining the overall pulse energy is needed for SRS measurements in gas-phase systems. One way to achieve this objective is to use a pulse-stretcher as described in this paper. The term 'pulse-stretcher' in this study is ideally suited for ns-long laser pulses and is different than the time-bandwidth-product type of pulse-stretcher that is routinely used in ultra-fast (femtosecond) laser systems.

Several concepts of pulse-stretching using electro-optical devices have been reported.<sup>10-14</sup> These other concepts were primarily intended to permit launching QS lasers pulses into optical fibers without damaging the fiber input faces. However, there are few pulse-stretching systems designed to reduce the high peak powers of ns-long 532 nm laser pulses from QS Nd:YAG lasers. Many of these techniques rely on complicated and often expensive electro-optic modulators to control the intra-cavity pulse buildup in the laser. Nguyen et al.<sup>6</sup> have previously demonstrated a pulse-stretching system for SRS excitation that uses beam splitters and mirrors in an optical ring-cavity configuration to stretch a laser pulse temporally. This pulse-stretcher was shown to be passive, reliable, and low cost compared to electro-optic schemes. Although this pulse-stretching technique works well and appears to be in demand for its utility in SRS spectroscopy in turbulent combusting flows,<sup>15</sup> the design and optimization of such a pulse-stretching system has not been previously described in detail in the literature.

In this paper we will present an analytical and experimental study of a laser pulse-stretching system that uses a series of optical ring-cavities. The results of this study will show the techniques used to design and optimize a reliable and passive pulse-stretching system for ns-long pulses. The goals of the optimization process are: minimizing peak laser power, avoiding laser-induced plasma spark generation, and avoiding damage to optical components in the beam path. These goals are then realized through a numerical calculation of the temporal and spatial

profiles of the stretched-pulses using the model. The results will clearly show the effects of key parameters such as: beam splitter reflectivity, optical cavity delay time, laser beam pointing instability, and laser beam divergence on the performance of the pulse-stretcher. The numerically optimized pulse-stretcher design will then be experimentally verified using a 3-cavity pulse-stretcher and a 1000 mJ/pulse QS Nd:YAG laser source.

## MODEL

The pulse-stretcher concept is based on a simple partially transmitting optical ring-cavity that is arranged in a right-triangle as shown in Fig. 1. Although other angles can be used, the right-triangle configuration permits the superposition of the input and output pulses upon exiting the cavity using readily available off-the-shelf 45° incidence beam splitters. The ring-cavity traps and stores a portion of the circulating laser pulse, subsequently releasing the stored pulse over a longer period of time as determined by the intra-cavity leakage rate  $(1-R_{BS})$ , where  $R_{BS}$  is the beam splitter reflectivity, and the optical delay time  $\tau$ , as determined by the optical propagation path length  $L$  in the optical cavity. From Fig. 1, if we follow the path of an 'original' laser pulse into the cavity, it is first partially reflected (by  $R_{BS}$ ) at the beam splitter. The remainder of the laser pulse is then transmitted (by  $1-R_{BS}$ ) through the beam splitter. The pulse then circulates inside the cavity for a time period  $\tau$ , and is then partially extracted via leakage through the beam splitter. The remainder of the pulse that is transmitted undergoes another round-trip in the cavity or is reflected/transmitted again, etc. The optical pulses exiting from the cavity have delay times given by  $\tau, 2\tau, \dots, k\tau$ , where  $k$  is an integer representing the number of round-trips in the cavity. Thus the ring-cavity divides an initially large amplitude laser pulse into many smaller amplitude pulses.

The pulses leaving one cavity can then be used as the input into other cavities to further stretch out the temporal profile of the laser pulse. Figure 2 shows a schematic of pulse-stretcher using three combined ring-cavities (1, 2, and 3). Each subsequent optical cavity divides an input pulse into multiple output pulses in the same way as the first cavity as shown in Fig. 1, with optical delay times given by:  $\tau_1$ ,  $\tau_2$ ,  $\tau_3$ , respectively. The multiple pulses created by these three cavities are subsequently recombined (a superposition in space and shifted in time) by the final beam splitter into an aggregate of many pulses, which appear as a single pulse with a longer temporal width. In general, subsequent cavities have shorter delay times ( $\tau_1 > \tau_2 > \tau_3$ ) to produce an aggregate series of pulses that appear to be one.

### Temporal Profile

The analytical model of the pulse-stretching process is based on Figs. 1 and 2. In order to simulate the temporal evolution of a laser pulse through the optical system, we first assume a Gaussian temporal laser pulse shape for the purposes of demonstrating this model. Although any arbitrary laser pulse shape can be used (through a fitted function), a Gaussian was found to closely approximate an injection-seeded QS laser pulse and is by definition, normalized. The instantaneous laser pulse power is then given by:

$$q(t) \equiv E \frac{2\sqrt{\ln(2)}}{\sqrt{\pi} d_t} \exp \left[ - \left( \frac{2\sqrt{\ln(2)} \cdot t}{d_t} \right)^2 \right] , \quad (1)$$

where  $q(t)$  has units of [J/s] or [W], and  $t$  is the time [s],  $E$  is the laser pulse energy [J],  $d_t$  is the temporal width of the laser pulse at full-width-half-maximum (FWHM) [s]. In order to general-

ize the model for an arbitrary laser pulse width, we then define the following non-dimensional parameters:

$$\chi \equiv \frac{t}{d_t} \quad , \quad (2a)$$

$$\Lambda \equiv \frac{E}{E_0} \quad , \quad (2b)$$

$$P_0 \equiv \frac{E_0}{d_t} \quad , \quad (2c)$$

$$\tau_i \equiv \frac{\Delta t_i}{d_t} \quad , \quad (2d)$$

$$\tau_{j,k} \equiv \frac{\Delta t_{j,k}}{d_t} \quad , \quad (2e)$$

where  $\chi$  is the non-dimensional time;  $\Lambda$  is the non-dimensional laser energy,  $E_0$  is normal unit energy [1 J];  $P_0$  is the unit-laser power based the laser pulse width  $d_t$ ;  $\Delta t_i$  is the round-trip propagation time for cavity  $i$  (“delay time”) [s];  $\tau_i$  is the non-dimensional delay time for cavity  $i$ ;  $\Delta t_{j,k}$  is the propagation time of light from cavity  $j$  to  $k$  [s]; and  $\tau_{j,k}$  is the non-dimensional transit time from cavity  $j$  to  $k$ . Using Eqns. (2a-2c) and normalizing Eqn. (1) by  $P_0$  following  $q(\chi d_t)/P_0 = Q(\chi)$ , we can rewrite Eqn. (1) in non-dimensional form as:

$$Q(\chi) \equiv \frac{\Lambda 2\sqrt{\ln(2)}}{\sqrt{\pi}} \exp\left[-\left(2\sqrt{\ln(2)} \cdot \chi\right)^2\right] , \quad (3)$$

which expresses the non-dimensional instantaneous laser power as a function of the non-dimensional time  $\chi$ . If we follow the path of a light pulse through the optical cavity shown in Fig. 1, we can see that the instantaneous output pulse power from cavity 1 ( $i = 1$ ) is then given by:

$$\begin{aligned} D_1(\chi) &= \overbrace{R_{BS} D(\chi)}^{\text{Initial Reflection}} + \overbrace{(1-R_{BS})^2 Q(\chi - \tau_1)}^{1^{\text{st}} \text{ pass}} + \overbrace{(1-R_{BS})^2 R_{BS} Q(\chi - 2\tau_1)}^{2^{\text{nd}} \text{ pass}} + \cdots + \overbrace{(1-R_{BS})^2 R_{BS}^{n-1} Q(\chi - n\tau_1)}^{n^{\text{th}} \text{ pass}} \\ &= R_{BS} Q(\chi) + (1-R_{BS})^2 \sum_{n=1}^N R_{BS}^{n-1} Q(\chi - n\tau_1) , \end{aligned} \quad (4)$$

where  $\tau_1$  is the non-dimensional delay time for cavity 1, and  $N$  is the number of round-trips of the laser pulse inside the cavity.  $D_0(\chi) = Q(\chi)$  for  $i = 1$ .  $D_1(\chi)$  then also represents the input pulse for the second cavity ( $i = 2$ ). Similarly, the instantaneous non-dimensional laser power from cavity 2 is then given by:

$$D_2(\chi) = R_{BS} D_1(\chi - \tau_{1,2}) + (1-R_{BS})^2 \sum_{m=1}^N R_{BS}^{m-1} D_1[\chi - (\tau_{1,2} + m\tau_2)] , \quad (5)$$

where  $\tau_2$  is the non-dimensional delay time for cavity 2, and  $\tau_{1,2}$  is the transit time from cavity 1 to cavity 2.

Eqns. (4 & 5) show a pattern that permits us to describe the instantaneous non-dimensional laser power from an arbitrary cavity  $i$  using the following recursion formula:

$$D_i(\chi) \equiv R_{BS} D_{i-1}(\chi - \tau_{i-1,i}) + (1-R_{BS})^2 \sum_{k=1}^N R_{BS}^{k-1} D_{i-1}[\chi - (\tau_{i-1,i} + k\tau_i)] , \quad (6)$$

where  $\tau_{0,1} = 0$  for  $i = 1$ . By substituting ( $i = 3$ ) into Eqn. (6), we produce an equation that describes  $D_3(\chi)$ , the instantaneous non-dimensional laser pulse profile of the final output from the 3-cavity pulse-stretcher system (we call the output of cavity 3 the “stretched-pulse”). Note that Eqn. (6) permits us to model a pulse-stretcher with an arbitrary number of optical cavities. For the purposes of most calculations, a cavity round-trip value of  $N = 10$  was found to give a good approximate convergence of the above summations, that is  $N = 10$  was sufficient to dissipate  $Q(\chi)$ . Although the analysis is non-dimensional, there are some parameters that eventually need to be evaluated based on real physical constraints such as the cavity-to-cavity propagation times as defined by Eqn. (2e). In the following calculations, we used  $\tau_{1,2} = 0.18$ , and  $\tau_{2,3} = 0.13$  as initial inputs unless another number was described. Note that the results of the analysis can easily be converted to real temporal units [s] by applying Eqn. (2a). That is, the non-dimensional axis ( $\chi$ ) represents actual time units in multiples of the FWHM of the input laser pulse width [s].

### Spatial Profile

A precise alignment of the optical ring-cavities in the pulse-stretcher is required to realize the best performance from the pulse-stretcher. However, in practice, it is difficult to align such a system perfectly by hand. Thus we need to estimate the effect of optical misalignment and shot-to-shot beam pointing instability on the pulse-stretcher performance in terms of the spatial profile of the resulting output pulse. We now examine how the spatial profile of the output pulse is affected by small angular deviations in the optical alignment, beam pointing stability and beam divergence. From Fig. 3, we can see that in the case of small deviations in the alignment of a mirror by an angle  $\pm \delta$ , will produce a lateral spatial displacement of the output beam profile by  $\pm L \tan(\delta)$  for a single round-trip of path length  $L$ . Note that  $\delta$  may have resulted from either

shot-to-shot beam pointing instability, or from a misalignment in one of the mirrors in the cavity which causes a successively larger lateral spatial shift in the position of the beam upon every round-trip inside the cavity. Moreover, the laser beam divergence represented by  $\theta$ , causes a gradual expansion of the beam diameter which grows with each round-trip within the cavity. Thus, the output beam diameter with a long optical propagation distance will be significantly larger than the input beam diameter purely from the effects of finite beam divergence as shown in Fig. 3. Thus the deviation angle  $\delta$ , and beam divergence  $\theta$  causes the spatial profile of the output beam to spread dramatically after passing through the pulse-stretcher.

We examine these effects numerically (assuming radial symmetry for simplicity) with the same model used for the temporal pulse profile but converted to the spatial domain using geometry and a  $\tan(\theta)$  transformation. First, the one-dimensional spatial profile of an original laser pulse (assumed to be a Gaussian function in space) is defined as:

$$q'(r, L) \equiv E \frac{2\sqrt{\ln(2)}}{\sqrt{\pi}(2 \tan \theta \cdot L + d_r)} \exp \left[ - \left( \frac{2\sqrt{\ln(2)} \cdot r}{(2 \tan \theta \cdot L + d_r)} \right)^2 \right] , \quad (7)$$

where  $q'(r, L)$  has units of [J/cm], and  $r$  is the radial position [cm],  $E$  is the laser pulse energy [J],  $d_r$  is the initial diameter of the original laser pulse at FWHM [cm],  $\theta$  is the beam divergence half-angle [rad], and  $L$  is the optical propagation distance [cm] (initially zero). In a manner similar to the previous temporal analysis, we then define the following non-dimensional parameters in order to generalize the results based on the spatial FWHM of the original laser pulse:

$$\rho \equiv \frac{r}{d_r} , \quad (8a)$$

$$\tilde{L}_i \equiv \frac{\Delta L_i}{d_r} \quad , \quad (8b)$$

$$\tilde{L}_{j,k} \equiv \frac{\Delta L_{j,k}}{d_r} \quad , \quad (8c)$$

where  $\rho$  is the non-dimensional radial position;  $\tilde{L}_i$  is the non-dimensional optical propagation distance for cavity  $i$  (initially zero);  $\Delta L_{j,k}$  is the optical propagation distance between cavity  $i$  and cavity  $j$  [cm];  $\tilde{L}_{j,k}$  is the non-dimensional optical propagation distance between cavity  $j$  and cavity  $k$ . Using Eqns. (2b & 8a - 8c), we recast Eqn. (7) in non-dimensional form as:

$$Q'(\rho, \tilde{L}_i) \equiv \Lambda \frac{2\sqrt{\ln(2)}}{\sqrt{\pi}(2 \tan \theta \cdot \tilde{L}_i + 1)} \exp \left[ - \left( \frac{2\sqrt{\ln(2)} \cdot \rho}{(2 \tan \theta \cdot \tilde{L}_i + 1)} \right)^2 \right] \quad , \quad (9)$$

From the recursion formula given by Eqn. (6), and given an incident laser pulse with a deviation angle  $\delta$  [rad] with respect to the original propagation ray angle, the one-dimensional spatial profile of the output pulse as a function of non-dimensional distance  $\rho$ , from an arbitrary cavity  $i$ , would be then given by the following recursion formula:

$$D'_i(\rho, \Psi_i) \equiv R_{BS} D'_{i-1}(\rho, \Psi_{i(n=0)}) + (1 - R_{BS})^2 \sum_{n=1}^N R_{BS}^{n-1} D'_{i-1}[\rho - (-1)^n \Psi_i \tan \delta, \Psi_i] \quad (10)$$

where  $\Psi_i$  is defined as equal to  $n\tilde{L}_i + \tilde{L}_{i-1,i}$ , the non-dimensional intra-cavity propagation distance, and  $D'_0(\rho, \Psi_i) = Q'(\rho, \tilde{L}_i)$ , and  $\tilde{L}_{0,1} = 0$  for  $i = 1$ . If we substitute ( $i = 3$ ) into Eqn. (10) we get a relation showing  $D'_3(\rho, \tilde{L}_3)$ , the non-dimensional spatial profile of the stretched output

pulse. The non-dimensional profile is easily converted to real units [J/cm] by applying Eqns. (2b & 8a).

## NUMERICAL OPTIMIZATION

For the purposes of optimizing the pulse-stretcher, we first assume a 3-cavity arrangement so that other parameters can be optimized initially. The pulse-stretcher described above has several parameters that can be varied, these include: (1) ratio of delay times for each cavity,  $\tau_1:\tau_2:\tau_3$  determined by the optical propagation distance in each cavity; (2) the delay time of cavity 1,  $\tau_1$  as it relates to the laser pulse width; and (3) the beam splitter reflectivity,  $R_{BS}$ . Once these parameters are optimized, we will then examine the last parameter, (4) the number of optical ring-cavities. We now examine each parameter to optimize and determine the ideal pulse-stretcher configuration.

### Effect of Cavity Delay Time Ratios

In order to examine the effect of the first parameter, the ratio of delay times on the efficacy of the pulse-stretcher, we try different combinations of cavity-delay ratios. Figure 4 shows the output pulse shapes from the pulse-stretcher for different ratios of delay times,  $\tau_1:\tau_2:\tau_3$ . A pulse in the case of  $\tau_1:\tau_2:\tau_3 = 4:2:1$  has a relatively smooth shape and lower peak power than others. Shapes of other pulses are highly distorted or bunched-up and oscillating. This result shows that delay time ratios which double in geometric progression, that is  $\tau_1:\tau_2:\tau_3 = 4n:2n:n$  (where  $n$  is integer), are best to recombine multiple pulses into a smooth single output pulse. From Fig. 4, it can be seen that using the proper cavity-delay ratios is critical in creating a smooth output pulse with the lowest possible peak power.

### Effect of Delay Time

We now investigate the effect of the second parameter, the delay time length on the efficacy of the pulse-stretcher. Figure 5 (a) shows variation of the peak laser power as a function of delay time. Fig. 5 (b) shows variation of the temporal pulse width of output pulses with changing of delay time,  $\tau_1$  from 1.0 to 7.5, and also shows the temporal pulse shape for  $\tau_1 = 6.5$  case. Here, the temporal width (FWHM) makes sense for "Gaussian-like" pulses, but not for highly distorted of oscillating pulse shapes such as shown in Fig. 4. So we choose the  $1/e^2$  standard for defining laser temporal pulse width for more consistency between different types of pulse shapes. As shown in Fig. 5 (a), the peak laser power decreases with an increase in  $\tau_1$  but it does not change very much past a  $\tau_1$  value of about 4. Note that the pulse width increases with an increase in the value of  $\tau_1$ . However, when  $\tau_1 > 5$ , the stretched output pulses do not recombine into a smooth pulse, but instead appear highly distorted in shape with multiple peaks that are over twenty times wider than the original pulse as shown in Fig. 5(b). As a result, a non-dimensional delay time of approximately  $\tau_1 = 4$  appears to be ideal for delay of the first cavity of a 3-cavity pulse-stretcher system. Based on this finding, and the fact that a 4:2:1 ratio for the different cavity delay times is best, we can see that the optimum pulse-stretcher cavity lengths (and delay times) are dictated completely by the input pulse width of the laser source. Thus, the shortest stage of the pulse-stretcher cavity should have a round-trip propagation time equal to the laser pulse temporal width  $d_t$  (FWHM) [ns]. Accordingly, subsequent longer-delay time cavities should double in geometric progression.

### Effect of Beam Splitter Reflectivity

We now look at the effect of beam splitter reflectivity on the performance of the pulse-stretcher. Figure 6 shows variations of the peak pulse power and the temporal width of output pulses with changes in the reflectivity of beam splitter,  $R_{BS}$  from 10% to 80%. From Figs. 5 and 6, it is clear that for an  $R_{BS}$  value of approximately 40% yields the best combination of lowest peak laser power and shortest overall pulse width. A short overall pulse width is desirable to minimize the optical cavity length. Thus, a 3-cavity optical configuration with the following parameters resulted in the optimum pulse-stretcher performance: delay time ratios  $\tau_1:\tau_2:\tau_3 \approx 4:2:1$ , initial delay time  $\tau_1 \approx 4$ , and beam splitter reflectivity  $R_{BS} \approx 40\%$ .

### Effect of Number of Cavities

Although for all the above calculations we have assumed a 3-cavity system (for the purposes of minimizing the physical size of the pulse-stretcher), we now consider how additional cavities in a pulse-stretcher affects the temporal profile of the stretched-pulse. Figure 7 shows the calculated laser pulse profiles for an original input laser pulse,  $Q(\chi)$  and the three different stretched output pulses:  $D(\chi)$  from a 2-cavity pulse-stretcher with  $\tau_1:\tau_2 = 2:1$  ( $\tau_1 = 2$ ) based on Eqn.(5);  $D(\chi)$  from a 3-cavity pulse-stretcher using the optimized optical parameters determined from the above exercise ( $\tau_1:\tau_2:\tau_3 = 4:2:1$ ,  $\tau_1 = 4$ ); and  $D(\chi)$  from 4-cavity pulse-stretcher with ( $\tau_1:\tau_2:\tau_3:\tau_4 = 8:4:2:1$ ,  $\tau_1 = 8$ ) based on Eqns. (3 - 6). From Fig. 7, we can clearly see that each additional cavity produces a longer and lower peak power stretched output pulse. We can also see that the optical configuration of the pulse-stretcher (via number of cavities, ratio of delay times, beam splitter reflectivity) permits us to manipulate temporal profile of laser pulse in many different ways.

However, the optical propagation distance becomes longer according to the total delay time of all cavities (i.e.  $\tau_1 + \tau_2 + \tau_3 + \dots$ ), so a 4-cavity pulse-stretcher will have beam divergence effects that become increasingly worse compared to a 3-cavity system. Furthermore, a 4-cavity system needs more physical area. For example, a 4-cavity system would require a 19.2 m long cavity-1 for an original laser pulse width  $d_t$  of 8 ns (FWHM). This kind of optical table space is prohibitively expensive (or unavailable in most laboratories). Thus, we chose 3-cavity arrangement for implementation based on a tradeoff between minimizing the size of the pulse-stretcher and the requirement that we reduce the peak power to 0.10X. Additionally, the 3-cavity system provides a relatively smooth and continuous output pulse profile (in time).

### **Spatial Profile Sensitivity**

Figure 8 shows the one-dimensional spatial profiles of the stretched-pulse including the effects of beam deviation and/or beam divergence as calculated from Eqn. (10). Here,  $\delta$  is assumed to be 25  $\mu\text{rad}$  based on the shot-to-shot beam pointing stability of a typical commercially available pulsed Nd:YAG laser, and the beam divergence,  $\theta$  is assumed to be 250  $\mu\text{rad}$  for the same product. From Fig. 8, we can see that beam deviation angle resulting from pointing instability does not significantly affect to the spatial profile of the output pulse when compared with the beam diameter. However, the beam divergence causes a significant spread in the spatial profile of the output pulse; the pulse spatial profile width at FWHM is approximately 2X the size of a beam that does not go through the pulse-stretcher system. This result indicates that stretched laser pulse diameter is significantly enlarged, and in theory, can affect the spatial resolution of the system in which it is implemented. However, in actual use, it really depends on how the stretched-pulse is eventually focused in the actual probe volume.

## EXPERIMENTAL

A goal of this study is develop a pulse-stretcher that produces a smooth, low-power Q-switched pulse that lasts at most, several hundred nanoseconds to permit sufficient temporal resolution for single-shot SRS measurements in subsonic flows. Another goal is to develop a pulse-stretcher that prevents laser-induced plasma generation. The laser-induced dielectric breakdown threshold for air at pressures ranging from approximately 1 to 4 atm using Q-switched Nd:YAG laser at 532 nm is of the order  $10^{12}$  to  $10^{13}$  W/cm<sup>2</sup> (with a negative pressure dependence).<sup>16</sup> Thus, the peak laser power needs to be kept below 0.08 GW in order to focus the laser beam down to a 0.1 mm diameter spot without generating a plasma spark. However, a more stringent requirement exists even prior to the smallest diameter beam-waist: preventing damage to optical windows/components in the focused beam path. The damage threshold of commercially available fused silica windows is ca. 1 GW/cm<sup>2</sup>. Often, long focal length (> 500 mm) lenses are used to focus the beam into the probe volume in order to produce a slender 1-d 'pencil-like' probe volume for the purposes of line-imaging. This produces a rather small beam diameter at the locations where the beam traverses an optical window, typically of the order 1 to 2 mm in diameter. Thus, the peak laser power must be kept below 0.02 GW if we wish to send a 1.5 mm diameter beam through fused silica. In short, we need to keep the laser peak power well below 0.02 GW to prevent window damage and to prevent plasma spark generation.

### Experimental Apparatus and Measurement

Figure 9 shows the optical layout of the pulse-stretcher used in this study to experimentally verify the analytical model. This arrangement employs three optical ring-cavities (1, 2, and 3) divided by three beam splitters. Here, the longer cavities are achieved by folding the optical path

with mirrors while still retaining the right-triangle arrangement. This particular design consists of eleven  $0^\circ$  incidence angle mirrors, five  $45^\circ$  (S-polarized) incidence angle mirrors, and three  $45^\circ$  (S-polarized) incidence beam splitters (partial reflectors). Note that the use of the right-triangle cavity arrangement permits us to use off-the-shelf optics for high efficiency reflection at angles close to  $0^\circ$  and  $45^\circ$ . Cavity 1, 2, and 3 perform three optical delays given by:  $\tau_1$ ,  $\tau_2$ , and  $\tau_3$ , respectively. Each delay time is equal to the propagation time of the light across the optical propagation distance [cm],  $L_1$ ,  $L_2$ , and  $L_3$  in each optical cavity. Note that extra attention has to be paid to using kinematic mirror mounts that are mechanically stable and possess a high degree of adjustment resolution in order to achieve the most reliable and trouble-free pulse-stretcher.

Figure 10 shows the simplified schematic illustrating how the pulse profiles were measured after each stage of delay. By simply inserting beam dumps at the locations shown, the following 4 cases were obtained:  $q(t)$  the reflection-only output pulse representing the original pulse,  $D_1(t)$  the output pulse from cavity 1 only,  $D_2(t)$  the output of cavities 1 and 2, and  $D_3(t)$  – the final stretched-pulse with no cavities blocked. All measurements were performed with the same optical layout and components as shown in Fig. 9, with the only differences implemented by blocking different cavities as shown in Fig. 10. This permits the relative intensities between the stretched and un-stretched pulses to be compared quantitatively. An injection seeded, Q-switched Nd:YAG laser (Spectra Physics, Quanta-Ray Pro-290) operating at 532 nm with about 1000 mJ/pulse was used as the laser source. The laser temporal pulse width was measured to be 8.4 ns (FWHM). The injection seeding feature is not required, but helps to produce a smooth pulse shape that is easier to model analytically (with a Gaussian function) and has better pulse-to-pulse energy stability with less timing-jitter. The stretched laser pulse emitted from the pulse-stretcher is directed onto a flat black-anodized aluminum plate which served as a beam dump.

The residual scattered light from the beam dump was attenuated using ND filters and detected with a fast (1 ns rise-time) Si-PIN photodiode (Thorlabs, DET-210). Output photo-currents from the photodiode, terminated into 50  $\Omega$ , were recorded with 9-bit resolution at 2.5 G-samples/sec using a digital oscilloscope (Tektronix, TDS-3032B).

### Numerical Model for Experimental Comparison

In order to compare experimental results with calculated results quantitatively, we calculated the stretched-pulse profile using the same optical parameters found in the experiment. For better accuracy of the resulting output pulse, we added the scattering losses at the anti-reflection (AR) coating surface ( $L_{AR}$ ) of the beam splitter, the reflectivity of the 0° mirror ( $R_{M0}$ ), and the reflectivity of the 45° mirror ( $R_{M45}$ ) which were ignored in the previous equations. Thus, the following “dimensional” equations were used to model the resulting stretched laser pulse based on Eqns. (1 & 4-6):

$$D_1(t) = (1 - L_{AR})^2 R_{BS} q(t) + (1 - L_{AR})(1 - R_{BS})^2 \sum_{n=1}^N [R_{M45} (R_{M0})^7]^n R_{BS}^{n-1} q(t - n\tau_1) \quad (11)$$

$$D_2(t) = (1 - L_{AR})^2 R_{M45} R_{BS} D_1(t - \tau_{12}) + (1 - L_{AR})(1 - R_{BS})^2 \sum_{m=1}^N [R_{M45} (R_{M0})^3]^m R_{BS}^{m-1} D_1[t - (\tau_{1,2} + m\tau_2)] \quad (12)$$

$$D_3(t) \equiv (1 - L_{AR})^2 R_{M45} R_{BS} D_2(t - \tau_{23}) + (1 - L_{AR})(1 - R_{BS})^2 \sum_{k=1}^N [R_{M45} R_{M0}]^k R_{BS}^{k-1} D_2[t - (\tau_{2,3} + k\tau_3)] \quad (13)$$

where  $t$  is the time [s];  $\tau_1$ ,  $\tau_2$ ,  $\tau_3$ ,  $\tau_{1,2}$ , and  $\tau_{2,3}$  now have dimensional units of [s].

For the experimental verification of the model, we used measured values for the following parameters:  $E = 1000$  mJ,  $d_t = 8.4$  ns,  $\tau_1 = 35.2$  ns,  $\tau_2 = 16.7$  ns,  $\tau_3 = 9.03$  ns,  $\tau_{1,2} = 1.53$  ns,  $\tau_{2,3} = 1.10$  ns,  $R_{BS1} = 40\%$ ,  $R_{BS2} = 41\%$ ,  $R_{BS3} = 40\%$ . Note that the delay time ratio of the actual pulse-stretcher was  $\tau_1 : \tau_2 : \tau_3 = 3.9 : 1.9 : 1$  (close to the ideal 4:2:1 ratio proposed in the previous section). The manufacturer's quoted mirror performance figures were used for the remaining parameters:  $L_{AR} = 0.25\%$ ,  $R_{M0} = 99.5\%$ , and  $R_{M45} = 99.0\%$  (CVI, Y2-Series high-energy mirrors).

### Quantitative Laser Pulse Analysis

Quantitative comparisons of the measured versus calculated pulse-stretcher profiles were realized by correcting the measured photodiode photocurrents against the optical transmittance of the series of beam splitters and mirrors. That is, the measured intensities of  $q(t)$ ,  $D_1(t)$  and  $D_2(t)$  given by Eqns. (1), (11), and (12), respectively were attenuated due to passage through the beam splitters ( $BS_1$ ,  $BS_2$  or  $BS_3$ ) and mirrors ( $M_1$  or  $M_2$ ). Thus, we corrected the measured intensity of  $q(t)$  by  $1/\alpha$ , where  $\alpha$  is the throughput efficiency of optics in Fig. 10, given by  $(R_{BS1} \cdot R_{M1} \cdot R_{BS2} \cdot R_{M2} \cdot R_{BS3})$ . Here  $R_i$  denotes the actual reflectivity of each beam splitter or mirror directly measured by a calibrated pyroelectric laser energy meter (Molelectron, J25LP-1) used with the laser operating in a long-pulse mode (ca. 2 mJ/pulse) to prevent damage to the energy meter. In the same manner, the measured time-varying power of the pulse represented by  $D_1(t)$  was corrected by  $1/\beta$ , where  $\beta$  is given by  $(R_{M1} \cdot R_{BS2} \cdot R_{M2} \cdot R_{BS3})$  and the measured intensity of  $D_2(t)$  was corrected by  $1/\gamma$ , where  $\gamma$  is given by  $(R_{M2} \cdot R_{BS3})$ . For the throughput efficiency of  $D_3(t)$ , all optics used in Fig. 9 were included in Eqn. (13).

All experimental data were calibrated using the scaling factor,  $\eta$ , where  $\eta$  is the conversion factor from photodiode voltage (across 50  $\Omega$ ) [V] to laser power [J/s] for the present ex-

perimental condition, to fit the peak power point of the measured original pulse,  $q(t)$  to the calculated laser pulse,. The measured  $q(t)$  signal was calibrated by delaying the signal during processing by  $(\tau_{1,2} + \tau_{2,3})$  to compensate for the fact that  $q(t)$  was measured just *after* BS<sub>3</sub> while the calculated  $q(t)$  means the one just *before* BS<sub>1</sub>. Thus, a quantitative representation of laser power versus time for the experimentally measured stretched-pulse was achieved.

## RESULTS AND DISCUSSIONS

Figure 11 shows the measured average and envelope temporal profile of the stretched-pulse for 256 shots. A relatively high variation in laser intensity of  $\pm 21\%$  against the mean value was observed for the period from 40 to 85 ns and variation of  $\pm 15\%$  was observed at the maximum point of intensity profile at 49 ns. These variations indicate that a factor of safety at least 15 % should be provided when selecting optical components such as mirrors or windows in the beam path following the pulse-stretcher, that may be damaged by higher peak pulse intensities. This factor of safety should also be included in the design of the minimum diameter of the beam waist to prevent optical breakdown of the gases at the focal point. This variation results partly from laser energy stability of  $\pm 3\%$ , and mainly from effects of minor optical cavity misalignment, shot-to-shot beam-pointing stability, and beam-divergence as shown in Fig. 8 which cause laser beam clipping at the edge of optics.

Figure 12 shows the comparison of measured temporal profiles (dotted line) of the original laser pulse and output pulses from the pulse-stretcher with numerically calculated profiles (solid line). As a result, the measured pulses for  $q(t)$ ,  $D_1(t)$ ,  $D_2(t)$ , and the stretched-pulse,  $D_3(t)$  show excellent agreement with the calculated pulses on overall shape. Figure 12 shows the evolution from a single original short pulse to a stretched-pulse. First, a single 8.4 ns-long FWHM pulse,  $q(t)$ , is divided into approximately six smaller pulses by cavity 1, shown by  $D_1(t)$ . Then,

the output of  $D_1(t)$  is divided to about eleven smaller pulses by cavity 2, shown by  $D_2(t)$ . Finally, the final pulse-stretcher output produces a much longer continuous pulse that is over 150 ns wide (approximately 75 ns half width) and reduces the peak laser power down to 0.011 GW from 0.11 GW, or 10% of the initial peak power. From Fig. 12(d) the stretched-pulse was found to maintain 82% of its initial laser energy by direct numerical integration of the experimentally measured stretched-pulse laser signal. This throughput efficiency value agrees extremely well with the result of  $83 \pm 5\%$  as directly measured by the pyroelectric energy meter (which does not account for the temporal shape of the pulse). This remarkable agreement shows that the calibration procedure outlined above indeed permits an accurate and quantitative comparison of the measured to calculated instantaneous laser power.

The inset curve in Fig 12(d) shows that the detailed profile of the experimentally measured stretched-pulse almost completely matches the calculated pulse for the period from 0 to 50 ns. However, the experimental data is about 25 % lower than the calculation in the decay curve portion of the pulse (after 80 ns) because of the combined effects of beam divergence and beam pointing instability as discussed previously. This effect becomes more prominent for the pulses that travel longer distances as the third and later peaks in the measured  $D_1(t)$  and  $D_2(t)$  profiles show slightly lower power than calculated profiles – the energy is simply lost due to beam clipping resulting from misalignment and divergence. Consequently, the experimentally measured stretched-pulse energy of 822 mJ is approximately 8% lower than predicted best total pulse energy of 933 mJ (limited only by mirror and beam splitter losses). This level of discrepancy is relatively minor and the accuracy of the model is sufficient for the purposes of designing and predicting pulse-stretcher performance. The majority of the energy losses result primarily from the limitations in the manual-alignment of the pulse stretcher system, and from the beam diver-

gence which causes beam clipping losses when the spatial profile of the beam exceeds the diameter of the optic component. We used 50 mm diameter optics for all mirrors and beam splitters in this study; with the 45° beam splitter, the clear aperture is reduced by  $1/\sqrt{2}$ . However, another option is to use larger diameter optics (say 75 mm) that reduces the effects of beam-clipping resulting from beam divergences. However, the cost of the optics become increasingly prohibitive with such large diameters.

## CONCLUSIONS

In this paper we described a simple and passive ns-long laser pulse-stretching system using multiple low-finesse optical ring-cavities utilizing a partially transmitting beam splitter. We modeled the pulse-stretching process with an expression that can be used to describe a pulse-stretcher containing an arbitrary number of optical cavities. Using the model, we optimized the design of a pulse-stretcher system suitable for use in a spontaneous Raman scattering excitation system that avoids the problematic laser-induced plasma spark problems that often accompany Q-switched Nd:YAG excitation sources. From the optimized design, we experimentally demonstrated and verified the model with a 3-cavity pulse-stretcher system that converts a 1000 mJ, 8.4 ns-long laser pulse into an approximately 150 ns-long (75 ns FWHM) output pulse with a peak power reduction of 0.10X, and an 83% efficiency. We found excellent agreement between model and experiment for the overall pulse profiles which indicates that the model can be used to accurately predict the performance for other general multi-cavity pulse-stretcher designs for the ns-long pulse regime. We also found that laser beam-pointing instability was a minor factor on the quality of the spatial profile of the output pulse, rather, the laser beam divergence and cavity

alignment were found to be much more critical. The following observations can be used as guidelines in the design of an optimized pulse-stretching system:

1. The cavity length (and delay time) for the optical cavities is dictated by input laser pulse width  $d_t$  (FWHM) [ns], and the shortest cavity delay time should equal the laser pulse width;
2. Longer delay time cavities preceding the shortest cavity should double in geometric progression, thus, for a 3-cavity system a 4:2:1 ratio should be used;
3. The optimum beam splitter reflectivity for the lowest peak-power, yet physically shortest cavity length is approximately 40%;
4. A 3-cavity system provides an approximate 0.10X reduction in peak power, with each additional cavity reducing the peak power by approximately an additional 50%.

*This work was supported principally by the Ultra-Efficient Engine Technologies (UEET) Program, and by the Zero CO<sub>2</sub> Emissions Technologies (ZCET) Program at NASA Glenn Research Center. This work was performed while the author held a National Research Council Research Associateship Award at NASA Glenn Research Center, funded by the UEET Program. The authors acknowledge the assistance of Mr. Raymond Lotenero in the construction of the pulse-stretcher system and its infra-structure. The authors acknowledge Dr. Robert Barlow, Sandia National Laboratories, Livermore CA, for his original design of the first pulse-stretcher of this type, and for his helpful suggestions.*

## REFERENCES

1. A. C. Eckbreth, *Laser Diagnostics for Combustion Temperature and Species*: 2<sup>nd</sup> Ed., Gordon and Breach Publishers, 209-273, (1996).
2. R. S. Barlow and C. D. Carter, "Raman/Rayleigh/LIF measurements of nitric oxide formation in turbulent hydrogen jet flames," *Combust. Flame* **97**, 261-280, (1994).
3. S. P. Nandula, T. M. Brown, R. W. Pitz, and P. A. DeBarber, "Single-pulse, simultaneous multipoint multispecies Raman measurements in turbulent nonpremixed jet flames," *Opt. Lett.* **19**:6, 414-416, (1994).
4. D. F. Marran, J. H. Frank, M. B. Long, S. H. Stårner, and R. W. Bilger, "Intracavity technique for improved Raman/Rayleigh imaging in flames," *Opt. Lett.* **20**:7, 791-793, (1995).
5. P. C. Miles, "Raman line imaging for spatially and temporally resolved mole fraction measurements in internal combustion engines," *Appl. Opt.* **38**:9, 1714-1732, (1999).
6. Q. V. Nguyen, R. W. Dibble, C. D. Carter, G. J. Fiechtner and R. S. Barlow, "Raman-LIF measurements of temperature, major species, OH, and NO in a methane-air bunsen flame," *Comb. Flame* **105**, 499-510, (1996).
7. F. Rabenstein, and A. Leipertz, "Two-dimensional temperature determination in the exhaust region of a laminar flat-flame burner with linear Raman scattering," *Appl. Opt.* **36**:27, 6989-6996, (1997).
8. L. J. Radziemski, and D. A. Cremers, editors, *Laser-Induced Plasma and Applications*, Marcel Dekker Inc., New York, (1989).
9. Y. -L. Chen, and J. W. L. Lewis, "Visualization of laser-induced breakdown and ignition," *Optics Express* **9**:7, 360-372, (2001).

10. G. Harigel, C. Baltay, M. Bregman, M. Hibbs, A. Schaffer, H. Bjelkhagen, J. Hawkins, W. Williams, P. Nailor, R. Michaels, and H. Akbari, "Pulse stretching in a Q-switched ruby laser for bubble chamber holography," *Appl. Opt.* **25**, 4102-4110, (1986).
11. S. Pflüger, M. Sellhorst, V. Sturm, and R. Noll, "Fiber-optic transmission of stretched pulses from a Q-switched ruby laser," *Appl. Opt.* **35**:25, 5165-5169, (1996).
12. M. Matsumoto, "Theory of stretched-pulse transmission in dispersion-managed fibers," *Opt. Lett.* **22**:16, 1238-1240, (1997).
13. V. Cautaerts, D. J. Richardson, R. Paschotta, and D. C. Hanna, "Stretched pulse  $\text{Yb}^{3+}$ :silica fiber laser," *Opt. Lett.* **22**:5, 316-318, (1997).
14. R. Engelhardt, R. Brinkmann, J. C. Walling, and D. F. Heller, "Pulse stretched solid-state laser lithotripter," United States Patent 5,496,306, (1996).
15. R. S. Barlow, and P. C. Miles, "A shutter-based line-imaging system for single-shot Raman scattering measurements of gradients in mixture fraction," *Proc. Combust. Inst.* **28**, 269-277, (2000).
16. X. T. Phuoc, "Laser spark ignition: experimental determination of laser-induced breakdown thresholds of combustion gases," *Opt. Comm.* **175**, 419-423, (2000).

## FIGURE CAPTIONS

Figure 1: Schematic of the basic right-triangle ring-cavity used as a pulse stretcher. The input laser pulse is divided into multiple smaller output pulses that are extracted through a partially transmitting beam splitter.

Figure 2: Schematic of a pulse-stretcher using multiple partially-transmitting optical ring-cavities (3-cavity arrangement). Legend: BS = beam splitter, M = mirror,  $\tau_i$  = a round-trip propagation time (delay time) for each ring-cavity,  $\tau_{i,j}$  = propagation time between two cavities.  $\tau_1 \geq \tau_2 \geq \tau_3$  in this study.

Figure 3: Schematic of the basic pulse-stretcher model with spatial pulse profile effects, including beam deviation,  $\delta$  and beam divergence,  $\theta$  (for cavity 1). Note that when  $\delta \ll 1$ , the optical path length  $L = L' = L''$ . Legend: BS = beam splitter, M = mirror.

Figure 4: Calculated output laser pulse shapes for different delay time ratios,  $\tau_1:\tau_2:\tau_3$ . Here, a beam splitter reflectivity of  $R_{BS} = 38\%$  was used and  $\tau_1 + \tau_2 + \tau_3 = 7$  was used as the constraint. The ordinate of the graph  $\Lambda/\chi$ , shows the non-dimensional laser power.

Figure 5: Calculated variations in the output pulse power and width as a function of cavity 1 delay times,  $\tau_1$ . (a) Effect on peak power, (b) effect on output pulse width. Here, the following parameters were used:  $\tau_1:\tau_2:\tau_3 = 4:2:1$ ,  $R_{BS} = 38\%$ . Note that the inset figure on (b) shows a pulse that has low peak power yet is highly oscillating in time and may be undesirable.

Figure 6: Calculated variations in output laser pulse power and width as a function of beam splitter reflectivity,  $R_{BS}$ . (a) Effect on peak power, (b) effect on pulse width.  $\tau_1:\tau_2:\tau_3 = 4:2:1$ ,  $\tau_1 = 4.2$ .

Figure 7: Calculated output profiles of with optimized parameters in a 2-, 3-, and 4-cavity arrangement.  $\tau_{1,2} = 0.1$ ,  $\tau_{2,3} = 0.1$ , and  $R_{BS} = 40\%$ . Integral of  $Q(\chi)$  or  $D_3(\chi)$  equal to  $\Lambda$ , that is  $\int Q(\chi)d\chi = \int D_3(\chi)d\chi = \Lambda$ . Each additional cavity provides an approximately 0.5X reduction in the peak laser power.

Figure 8: Calculated 1-dimensional spatial profiles of the stretched output pulse that include the effects of laser beam angular deviation and/or divergence compared with a system that has “perfect alignment”. The graph ordinate,  $\Lambda/\chi$  shows the non-dimensional laser power. The original laser beam is assumed to be spatially Gaussian with a FWHM diameter of one unit of  $\rho$ .  $\delta = 25\ \mu\text{rad}$  and  $\theta = 250\ \mu\text{rad}$ . Note that with “perfect alignment” both of  $\delta$  and  $\theta$  are equal to 0. The integral of each profile equals  $\Lambda$ .

Figure 9: Schematic of the experimental layout of the 3-cavity pulse-stretcher used (each cavity is delimited by the beam splitter). The whole system (for about 11 m optical length in the first stage) can be assembled onto a standard 1.52 m (5 ft) x 0.91 m (3 ft) optical breadboard using folding mirrors as shown.

Figure 10: Schematic of the experimental arrangement used for the pulse-stretching measurements. In measurement of  $q(t)$ , all cavities blocked; in measurement of  $D_1(t)$ , cavities 2 and 3 blocked; in measurement of  $D_2(t)$ , only cavity 3 blocked; in stretched-pulse measurement, no cavities blocked. Legend:  $M_i$  = mirrors,  $BS_i$  = beam splitter,  $C_i$  = ring-cavity, PD = photo diode, BD = Beam dump, OSC = Oscilloscope, SP = Scattering plate (beam dump).

Figure 11: Measured temporal profile of the stretched-pulse output using the 3-cavity pulse-stretcher shown in Fig. 9. The 'Envelope' shows shot-to-shot variations for 256 shots (from minimum to maximum). The graph ordinate shows photo diode currents (V into 50  $\Omega$ ), representing laser intensity as a function of time.

Figure 12: Temporal profiles of measured and calculated laser pulses. (a)  $q(t)$ : Original pulse, (b)  $D_1(t)$ : output pulse from cavity 1 only, (c)  $D_2(t)$ : output pulse from cavity 2 (after passing through cavity 1 and 2), (d)  $D_3(t)$ : final output or 'stretched-pulse'. Solid line (—) represents the calculation and the dotted line (⋯) is experimental data. In both experiment and calculation,  $d_t = 8.4$  ns,  $\tau_1 = 35.2$  ns ( $\tau_1 / d_t = 4.2$ ),  $\tau_1 : \tau_2 : \tau_3 = 3.9 : 1.9 : 1$ ,  $\tau_{1,2} = 1.53$  ns,  $\tau_{2,3} = 1.10$  ns,  $R_{BS} \approx 40$  %. In calculation,  $N = 6$  and  $E = 1000$  mJ. The experimental data is averaged over 256 shots. The output energy of both the measured and calculated stretched-pulses are obtained by direct integration of the profiles in time. Note that the residual signal in the tail portion (30 - 45 ns) of  $q(t)$  as measured in (a) is most likely the result of a minor electrical impedance mismatch which shows up as a minor ringing.

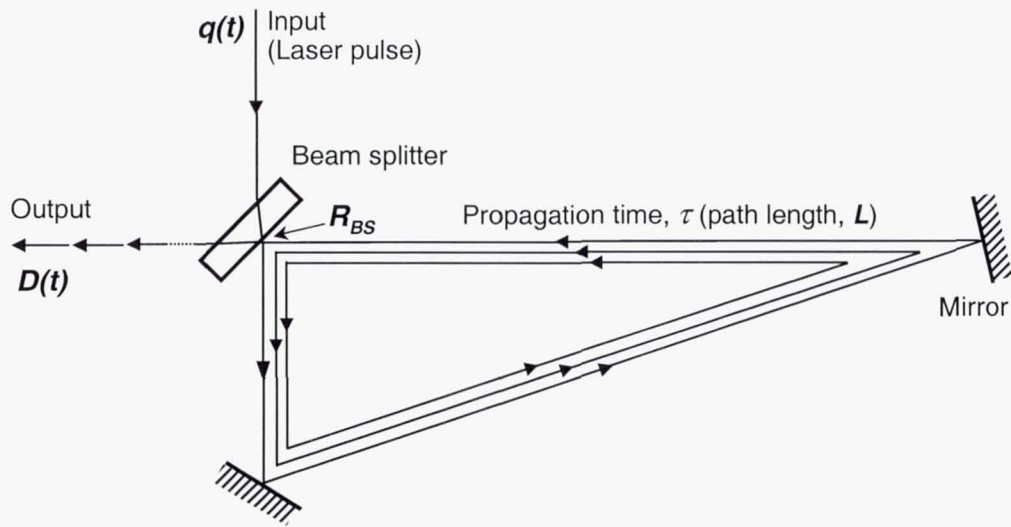


Figure 1

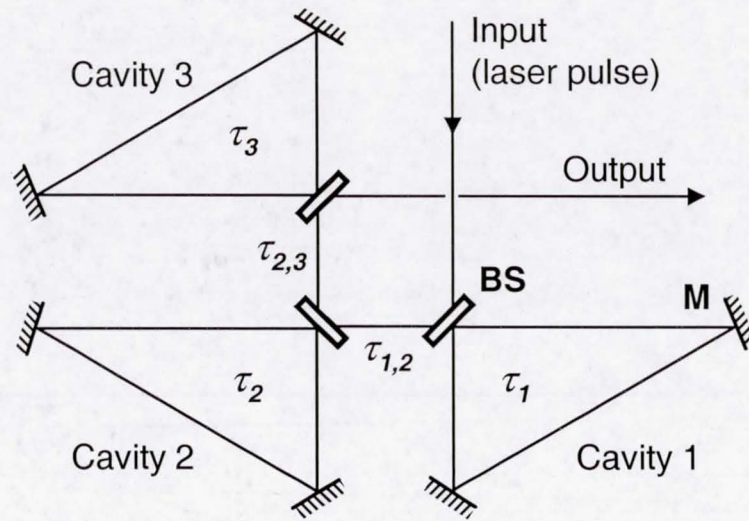


Figure 2

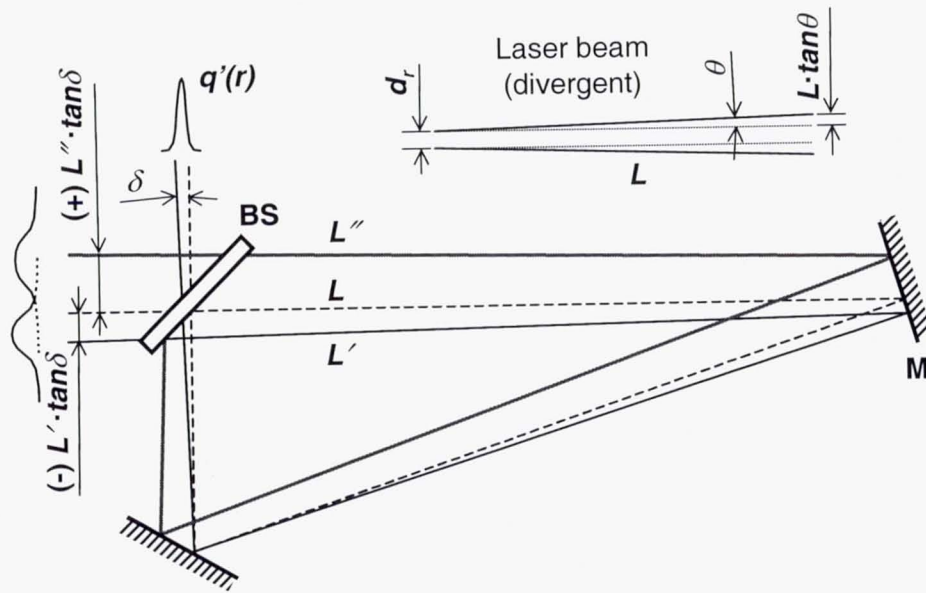


Figure 3

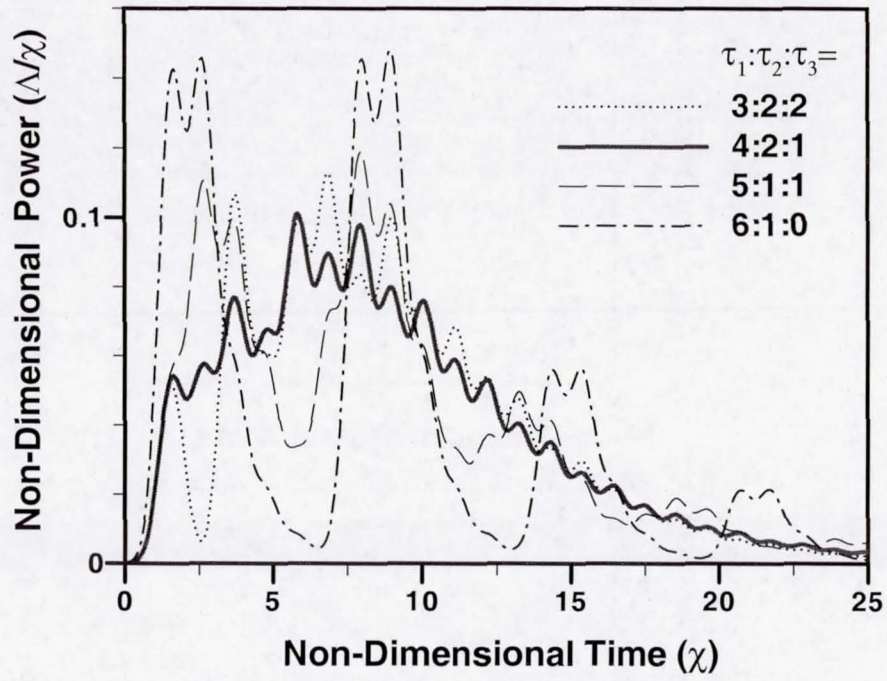


Figure 4

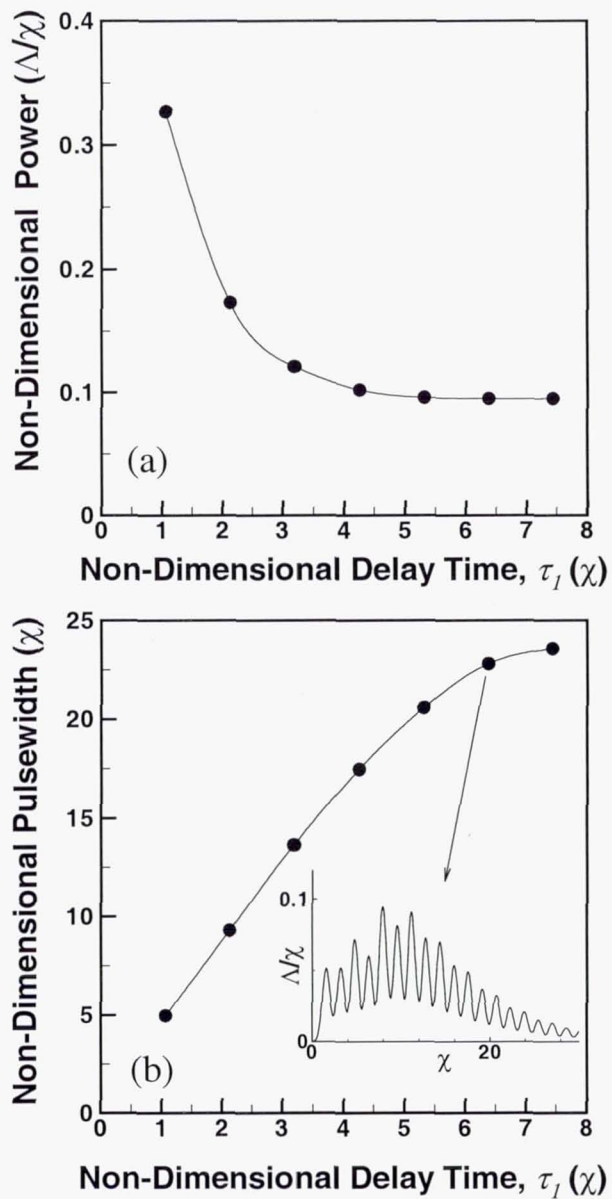


Figure 5

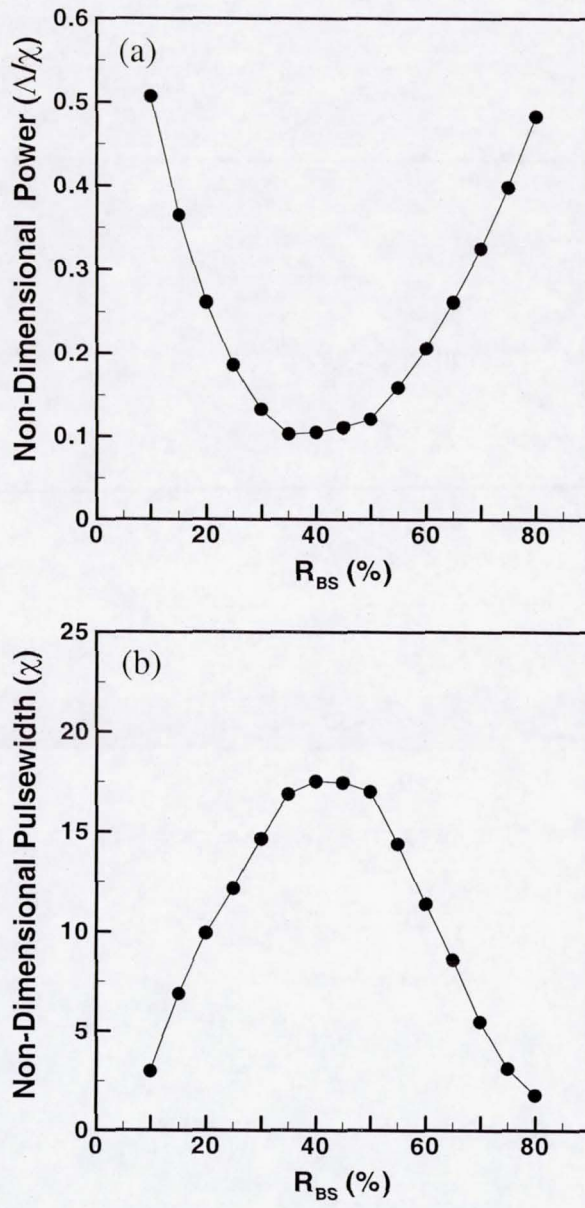


Figure 6

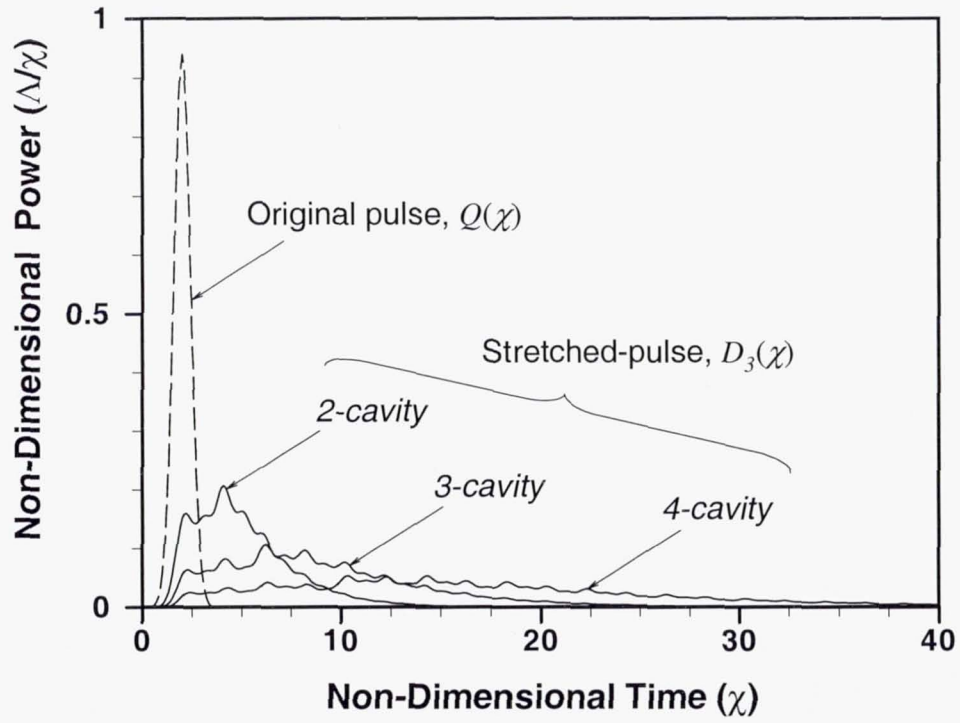


Figure 7

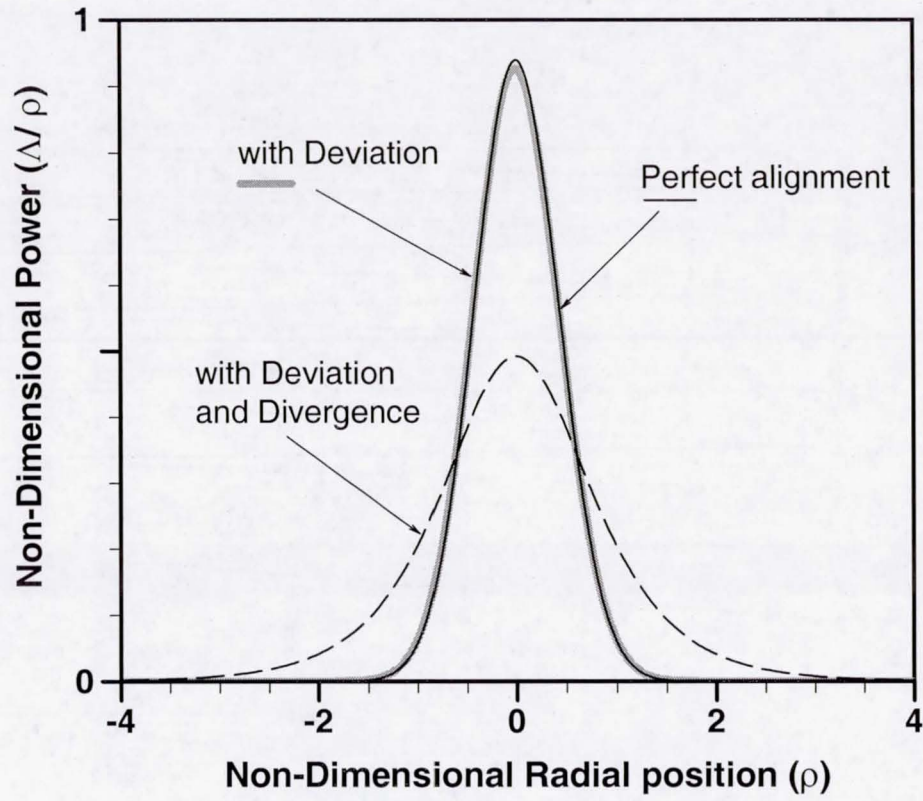


Figure 8

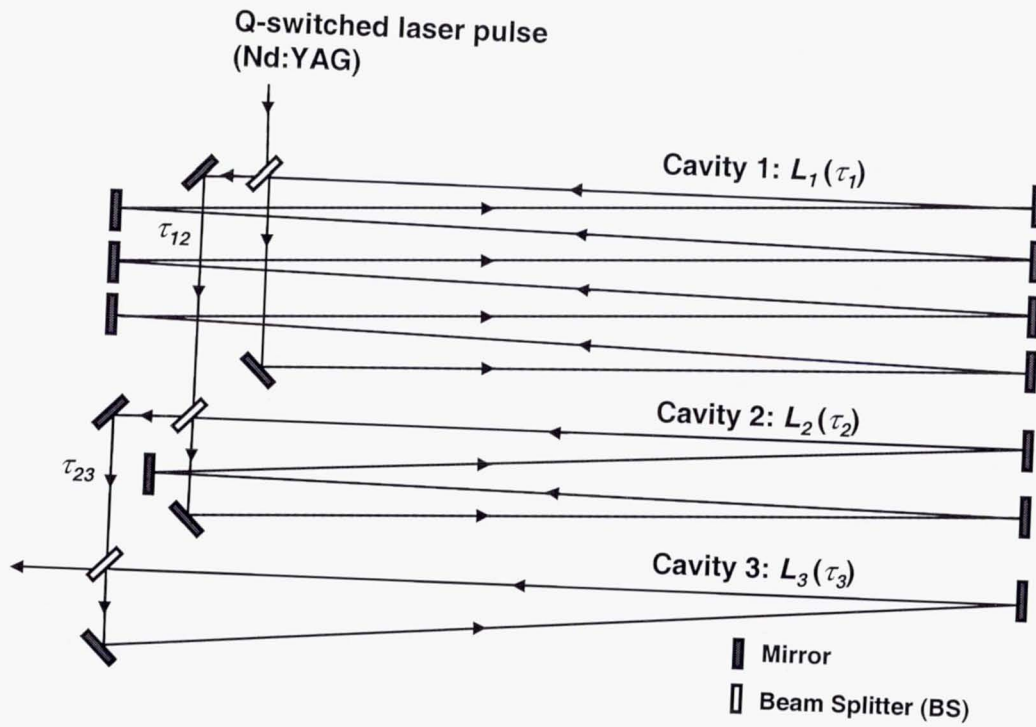


Figure 9

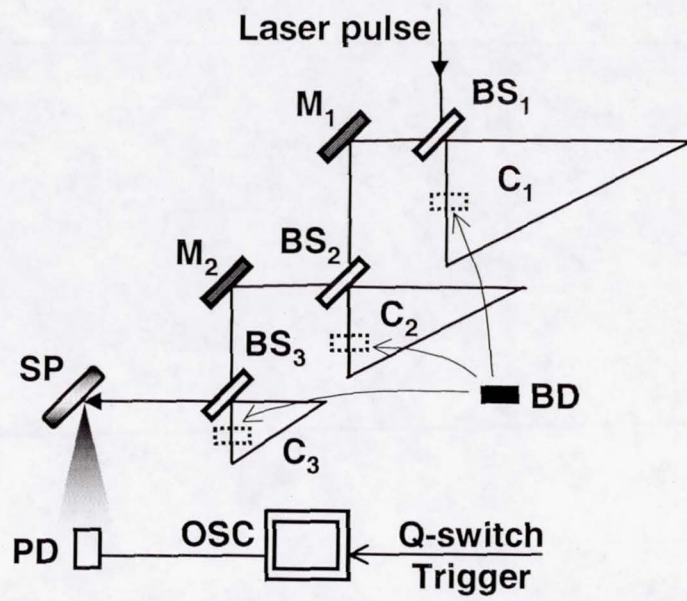


Figure 10

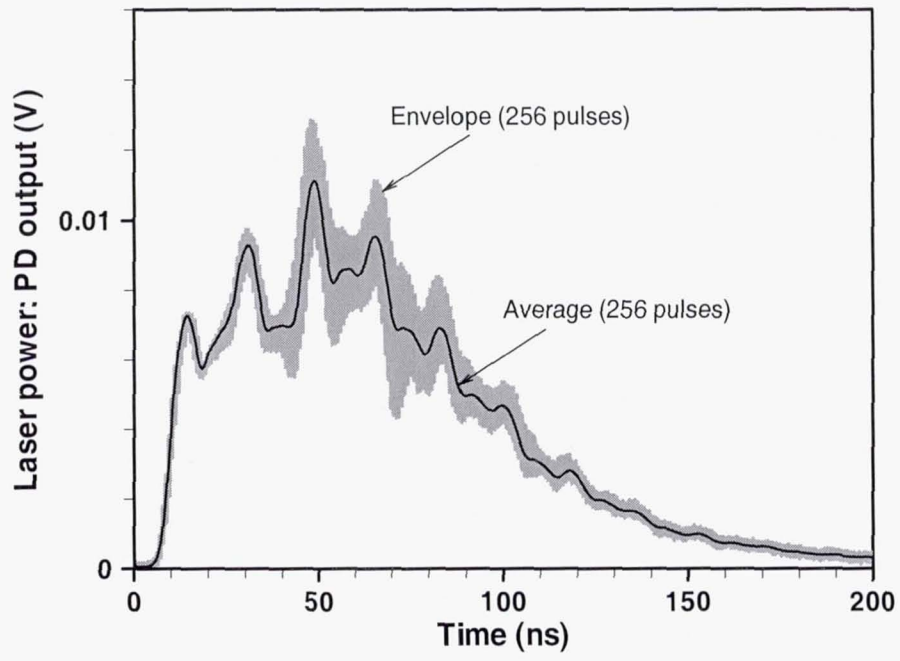


Figure 11

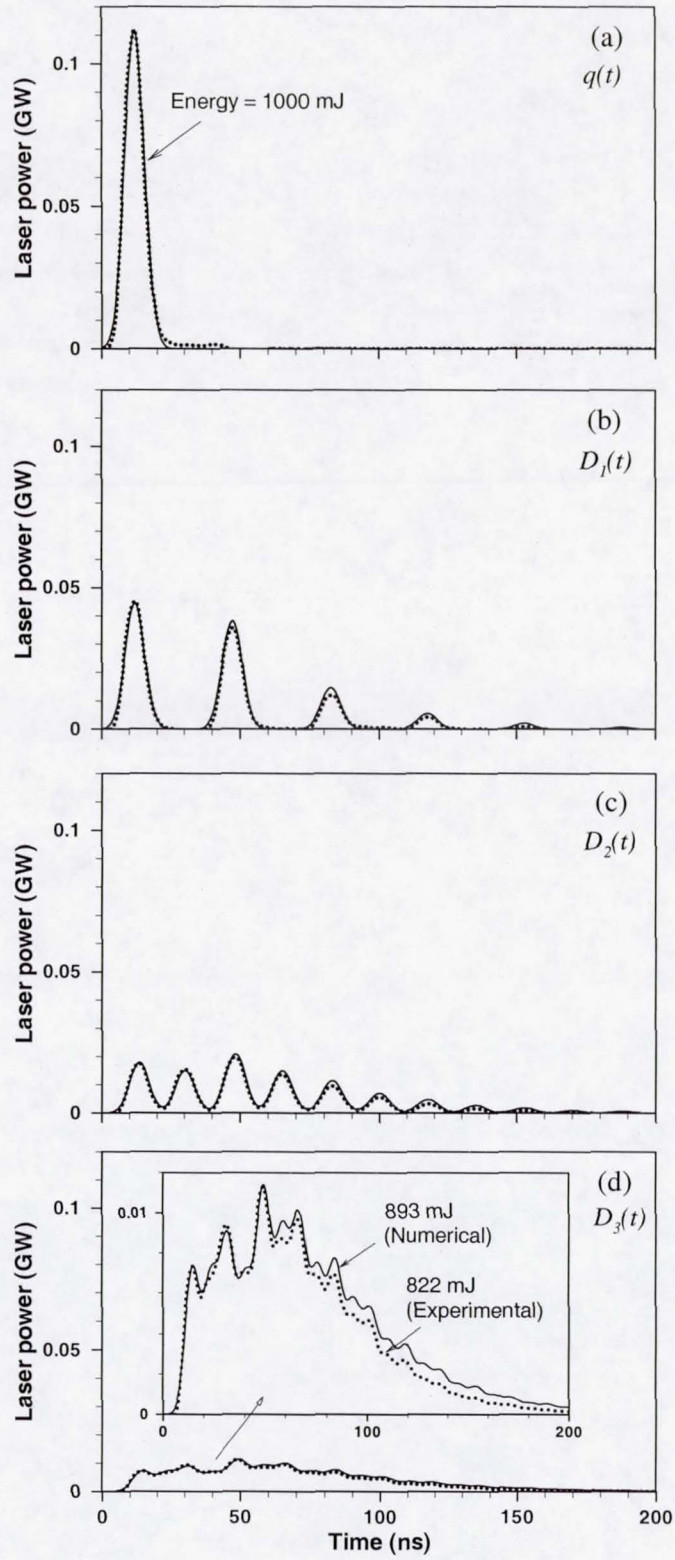


Figure 12